



# Trace Ru atoms implanted into a Ni/Fe-based oxalate solid-solution-like with high-indexed facets for energy-saving overall seawater electrolysis assisted by hydrazine

Jiayang Zhao<sup>a</sup>, Haoran Guo<sup>a</sup>, Qinghua Zhang<sup>b</sup>, Yanyan Li<sup>a</sup>, Lin Gu<sup>b,\*</sup>, Rui Song<sup>a,\*\*</sup>

<sup>a</sup> School of Chemical Sciences, University of Chinese Academy of Sciences, 19 Yuquan Road, Shijingshan District, Beijing 100049, PR China

<sup>b</sup> Key Laboratory for Renewable Energy, Beijing Key Laboratory for New Energy Materials and Devices, Laboratory of Advanced Materials and Electron Microscopy, Beijing National Laboratory for Condensed Matter Physics, Institute of Physics, Chinese Academy of Sciences, 8 South 3rd Street, Zhongguancun, Haidian District, Beijing 100190, PR China

## ARTICLE INFO

### Keywords:

Ru modification  
Ni/Fe-oxalate solid solution  
Hydrazine oxidation reaction  
Energy-saving hydrogen production  
Overall seawater splitting

## ABSTRACT

Seawater splitting is considered as an economically appealing yet technically challenging approach to generate hydrogen fuel. Hampered by the sluggish oxygen evolution reaction (OER) and the detrimental effects of chlorine electrochemistry, designing robust and highly efficient electrocatalysts for the hydrogen evolution reaction (HER) in parallel with the hydrazine oxidation reaction (HzOR) is extremely imperative for hydrogen production in seawater mediums. Herein, we present a protocol that implants Ru nanospecies into a Ni/Fe-oxalate solid-solution-like with high-indexed facets to engineer an effective and novel-structured catalyst (Ru-(Ni/Fe)<sub>2</sub>O<sub>4</sub>). Systematic experimental analyses alongside the theoretical calculations reveal that the synergistic effect of Ru nanospecies and high-index facets from (Ni/Fe)<sub>2</sub>O<sub>4</sub> endows Ru-(Ni/Fe)<sub>2</sub>O<sub>4</sub> with extraordinary activities of HER, OER and HzOR. When assembled into an electrolyzer, the cell voltage reduces to 0.01 V at 10 mA cm<sup>-2</sup> for HER-HzOR coupling seawater splitting. Moreover, the system remains stable under 500 mA cm<sup>-2</sup> at 80 °C for 50 h, almost meeting the requirements for quasi-industrial electrolysis. This work proposes a guideline for preparing multifunctional electrocatalysts and provides an effective strategy for developing seawater electrolysis to achieve a hydrogen economy society.

## 1. Introduction

Electrochemical water splitting is one of the promising pathways for large scale hydrogen production, including hydrogen evolution reaction (HER:  $2\text{H}_2\text{O} + 2\text{e}^- \rightarrow \text{H}_2 + 2\text{OH}^-$ , 0 V vs. RHE) and oxygen evolution reaction (OER:  $4\text{OH}^- - 4\text{e}^- \rightarrow 2\text{H}_2\text{O} + \text{O}_2$ , 1.23 V vs. RHE) [1]. Currently, traditional water electrolyzers are heavily dependent on scarce freshwater, which markedly reduces the possibility of large-scale electrolysis [2]. In this context, it is indispensable to use seawater as feedstock, which is deemed an inexhaustible water resource [3]. Unfortunately, direct seawater electrolysis faces formidable technological challenges. Particularly, the chlorine evolution reaction (ClER:  $\text{Cl}^- + 2\text{OH}^- \rightarrow \text{ClO}^- + \text{H}_2\text{O} + 2\text{e}^-$ , 1.71 V vs. RHE) competes with OER at the anode, which not only jeopardizes the Faradaic efficiency of the OER but also generates  $\text{ClO}^-$  to poison the catalysts [4,5]. On the other hand, the

OER with a four-electron-transfer reaction shows sluggish kinetics and high thermodynamic potential, resulting in a large energy demand [6, 7]. To circumvent these difficulties, substituting the sluggish OER with thermodynamically favorable small-molecule oxidation reactions is one of the most promising avenues [8,9]. Among many alternative reactions, the hydrazine oxidation reaction (HzOR:  $\text{N}_2\text{H}_4 + 4\text{OH}^- \rightarrow \text{N}_2 + 4\text{H}_2\text{O} + 4\text{e}^-$ , -0.33 V vs. RHE) can negatively shift the anodic potential to avoid the occurrence of ClER [10,11]. Assisted by HzOR, the overall seawater electrolysis only generates  $\text{N}_2$  and  $\text{H}_2$ , which effectively avoids the notorious problems of  $\text{H}_2/\text{O}_2$  risky gas and chlorine chemistry in the electrolyzer [12,13]. Nevertheless, the slow reaction kinetics of the HzOR and limited gas-liquid diffusion kinetics make the potential much higher than the theoretical value [14–16]. Thereupon, exploring effective and steady bifunctional electrocatalysts for the HzOR and HER is keenly compelling but challenging.

\* Correspondence to: Institute of Physics, Chinese Academy of Sciences.

\*\* Correspondence to: School of Chemical Sciences, University of Chinese Academy of Sciences.

E-mail addresses: [l.gu@iphy.ac.cn](mailto:l.gu@iphy.ac.cn) (L. Gu), [rsong@ucas.ac.cn](mailto:rsong@ucas.ac.cn) (R. Song).

To date, the state-of-the-art electrocatalysts are still noble metals including Pt, Pd and Ir, while their scarcity and low durability dramatically impede industrial applications [17–19]. NiFe-based materials have been brought to the forefront due to their outstanding OER properties [20,21]. However, the primary bottleneck of Ni/Fe-based materials recently developed lies in their poor stability and HER performance, and there are relatively few studies on their catalytic properties in the HzOR [22,23]. As a coordination polymer, Ni/Fe-based oxalate has the advantages including a highly ordered structure and high synthetic designability, which is expected to be the ideal model electrocatalyst [24,25]. It has been reported that the active sites for the HER are mainly low-valenced metals, while the active sites for the HzOR are mainly from high-index facets (HIFs) [26,27]. Based on these concerns, integrating low-valenced metals with NiFe-based oxalate HIFs may be a promising method for the simultaneous regulation of HER and HzOR properties. Nevertheless, due to the inherently high surface energies, it is normally difficult to prepare HIFs at a large scale [28,29]. On the other hand, Ru, the cheapest platinum-group metal, is considered the metal with the most potential to enhance electrocatalytic properties [30,31]. However, Ru shows poor stability in the electrocatalytic process due to irreversible agglomeration and poor tolerance [32,33]. Therefore, it is laborious, but desirable, to finely fabricate bifunctional electrocatalysts by doping Ru into NiFe-based oxalate along with HIFs.

Herein, we bring forward a new strategy to construct a Ru-modified Ni/Fe-based oxalate solid-solution-like (Ru-(Ni/Fe) $\text{C}_2\text{O}_4$ ). Initially, Ni/Fe-based oxalate solid-solution-like ((Ni/Fe) $\text{C}_2\text{O}_4$ ), with a mix of Ni and Fe elements atomically, is in situ grown on the surface of Ni foam by impregnation. The (Ni/Fe) $\text{C}_2\text{O}_4$ , consisting of the abundant HIFs of  $\text{NiC}_2\text{O}_4$  and  $\text{FeC}_2\text{O}_4$ , is stacked from nanoparticles (0D), microbelts (2D), and micropriams (3D). Then, Ru species are implanted into (Ni/Fe) $\text{C}_2\text{O}_4$  by the reaction of  $\text{Ru}^{3+}$  and  $\text{C}_2\text{O}_4^{2-}$  to engineer an effective and novel catalyst during the solvothermal reaction. The combination of experiments and theoretical calculations indicate that the synergistic effect of Ru nanospecies and high-index facets from (Ni/Fe) $\text{C}_2\text{O}_4$  endow Ru-(Ni/Fe) $\text{C}_2\text{O}_4$  with extraordinary electrocatalytic activities of HER, OER and HzOR in alkaline media. Moreover, the experimental results demonstrate that implanting Ru nanospecies can stabilize the HIFs from (Ni/Fe) $\text{C}_2\text{O}_4$  via forming a relatively strong bond of Ru–M, which effectively protects Ni/Fe atoms from dissolution in a hybrid alkaline electrolyzer. Impressively, the two-electrode configuration assembled by Ru-(Ni/Fe) $\text{C}_2\text{O}_4$  as both the anode and cathode present preminent performance in overall seawater electrolysis assisted by hydrazine, which only requires a potential of 0.01 V to reach 10 mA  $\text{cm}^{-2}$  and remains stable at quasi-industrial conditions for 50 h. This work not only discloses the feasibility of combining metal dopants and HIFs to improve the electrocatalytic properties but also provides an effective strategy for the scientific and technological development of overall seawater electrolysis.

## 2. Experimental section

### 2.1. Synthesis of (Ni/Fe) $\text{C}_2\text{O}_4$

The (Ni/Fe) $\text{C}_2\text{O}_4$  self-supporting electrode was prepared via a simple and easy-scale impregnation procedure. Prior to the synthesis, a piece of commercial Ni foam (NF, 3 cm  $\times$  2 cm  $\times$  0.2 mm) was ultrasonically washed with 3 M HCl, acetone, ethanol, and deionized water for 15 min in sequence. Then, the fresh NF was immersed into a 20 mL 1 M  $\text{H}_2\text{C}_2\text{O}_4$  aqueous solution dissolved with 0.6 mmol  $\text{FeCl}_3 \cdot 6\text{H}_2\text{O}$  at room temperature for 3 h. After that, the sample was taken out and dried to obtain (Ni/Fe) $\text{C}_2\text{O}_4$ .

### 2.2. Synthesis of Ru-(Ni/Fe) $\text{C}_2\text{O}_4$

The as-synthesized (Ni/Fe) $\text{C}_2\text{O}_4$  was transferred into a 50 mL Teflon-lined stainless-steel autoclave containing 30 mL ethanol solution and 75

mg  $\text{RuCl}_3 \cdot 3\text{H}_2\text{O}$ . Afterward, the autoclave was sealed and maintained at 120  $^\circ\text{C}$  for 3 h. The resultant sample was rinsed with ethanol several times, followed by drying in a vacuum oven at 40  $^\circ\text{C}$  for 6 h, and labeled as Ru-(Ni/Fe) $\text{C}_2\text{O}_4$ .

The materials characterizations and the parameters of electrochemical measurement are supplied in Supporting Information (SI).

## 3. Results and discussion

### 3.1. Structure characterization

The synthetic strategy for Ru-(Ni/Fe) $\text{C}_2\text{O}_4$  is schematically depicted in Fig. 1a (see the Experimental Section for details). Initially, facile and gentle impregnation is conducted on the substrate of conductive Ni foam (NF, Fig. S1). As an oxidizing agent and pH regulator,  $\text{FeCl}_3$  reacts with NF to generate  $\text{Fe}^{2+}$  and  $\text{Ni}^{2+}$ , and then both further bond with  $\text{C}_2\text{O}_4^{2-}$  to form (Ni/Fe) $\text{C}_2\text{O}_4$  in situ. Subsequently, trace Ru species are implanted into (Ni/Fe) $\text{C}_2\text{O}_4$  by the reaction of  $\text{Ru}^{3+}$  and partial  $\text{C}_2\text{O}_4^{2-}$  during the following solvothermal reaction to form the desired Ru-(Ni/Fe) $\text{C}_2\text{O}_4$  electrocatalyst. All materials are uniformly grown on the NF, as shown in Fig. S2.

The X-ray diffraction (XRD) pattern is firstly collected to probe the crystalline phase structure in Fig. 1b. The sharp peaks at 18.4 $^\circ$ , 22.9 $^\circ$ , 29.1 $^\circ$ , 34.3 $^\circ$ , 37.4 $^\circ$ , 42.8 $^\circ$ , 45.8 $^\circ$ , 48.2 $^\circ$ , and 57.3 $^\circ$  correspond to the (202), (004), (400), (022), (206), (224), (602), (026) and (426) planes of orthorhombic  $\beta\text{-FeC}_2\text{O}_4 \cdot 2\text{H}_2\text{O}$  (JCPDS 22–0635) [34]. The diffraction peaks at 18.5 $^\circ$ , 29.0 $^\circ$ , 30.1 $^\circ$ , 35.3 $^\circ$ , 43.3 $^\circ$ , 48.7 $^\circ$ , and 58.0 $^\circ$  coincide well with the (202), (114), (400), (022), (512), (026) and (332) planes of orthorhombic  $\beta\text{-NiC}_2\text{O}_4 \cdot 2\text{H}_2\text{O}$  (JCPDS 25–0582). Meanwhile, the peaks at 18.8 $^\circ$ , 30.4 $^\circ$ , 40.3 $^\circ$ , and 47.7 $^\circ$  match the (–202), (–402), (–314) and (604) planes of monoclinic  $\alpha\text{-NiC}_2\text{O}_4 \cdot 2\text{H}_2\text{O}$  (JCPDS 25–0581) [35]. Noticeably, the adjacent location of diffraction peaks and the nearly consistent lattice parameters of  $\text{FeC}_2\text{O}_4 \cdot 2\text{H}_2\text{O}$  and  $\text{NiC}_2\text{O}_4 \cdot 2\text{H}_2\text{O}$  (Fig. S3) indicate the blending of  $\text{NiC}_2\text{O}_4$  and  $\text{FeC}_2\text{O}_4$  at an atomic level to form solid-solutions-like [36]. Significantly, the XRD pattern of Ru-(Ni/Fe) $\text{C}_2\text{O}_4$  displays an almost identical pattern, implying that the incorporation of Ru species hardly alters the crystalline orientations. The morphology was then characterized by scanning electron microscopy (SEM). Fig. 1c shows that (Ni/Fe) $\text{C}_2\text{O}_4$  comprises a multitude of prism-shaped microstructures (micropriams) with an average width of  $\sim$ 800 nm and length of  $\sim$ 1  $\mu\text{m}$ , which are uniformly and vertically grown on the NF. The optimization process of the samples is shown in Figs. S4, 5, 6 and 7. The energy-dispersive X-ray spectroscopy (EDS) result in Fig. S8 illustrates the homogeneous distributions of Ni, Fe, C and O. The panoramic SEM image of Ru-(Ni/Fe) $\text{C}_2\text{O}_4$  demonstrates basically unchanged geometries and dimensions after the solvothermal reaction (Fig. 1d). Notably, a single micropriam shows the more obvious hierarchical structure, i.e., micropriams stacked from microbelts. The EDS result in Fig. S9 shows the successful incorporation of Ru. By controlling the same loading amounts of Ru, Ru-modified NF (Ru-NF) is prepared for comparison (Figs. S10 and 11). Afterward, transmission electron microscopy (TEM) was conducted to validate the stacking structure. The representative TEM image in Figs. 1e and S12 reveals that (Ni/Fe) $\text{C}_2\text{O}_4$  is shaped with microbelts, confirming the aforementioned stacking structure. Of particular interest, the microbelt is also stacked by numerous nanoparticles with an average diameter of  $\sim$ 4.8 nm. The  $\text{N}_2$  desorption pore volume distribution curve in Fig. S13 shows that most pore sizes are distributed at  $\sim$ 1.2 nm, which provides a suitable precursor for loading Ru species in the following process. The TEM image of Ru-(Ni/Fe) $\text{C}_2\text{O}_4$  in Figs. 1f and S14 depicts the unchanged microbelt structure stacked from nanoparticles. Moreover, the high-resolution TEM (HRTEM) image in region I shows the (–114) plane of  $\text{NiC}_2\text{O}_4$  and the (202) plane of  $\text{FeC}_2\text{O}_4$ , and that in region II shows the (512) plane of  $\text{NiC}_2\text{O}_4$  and the (004) plane of  $\text{FeC}_2\text{O}_4$  [37,38]. These interlacing high-index facets (HIFs) of  $\text{NiC}_2\text{O}_4$  and  $\text{FeC}_2\text{O}_4$  validate the successful formation of a solid-solution-like, which is in line with XRD



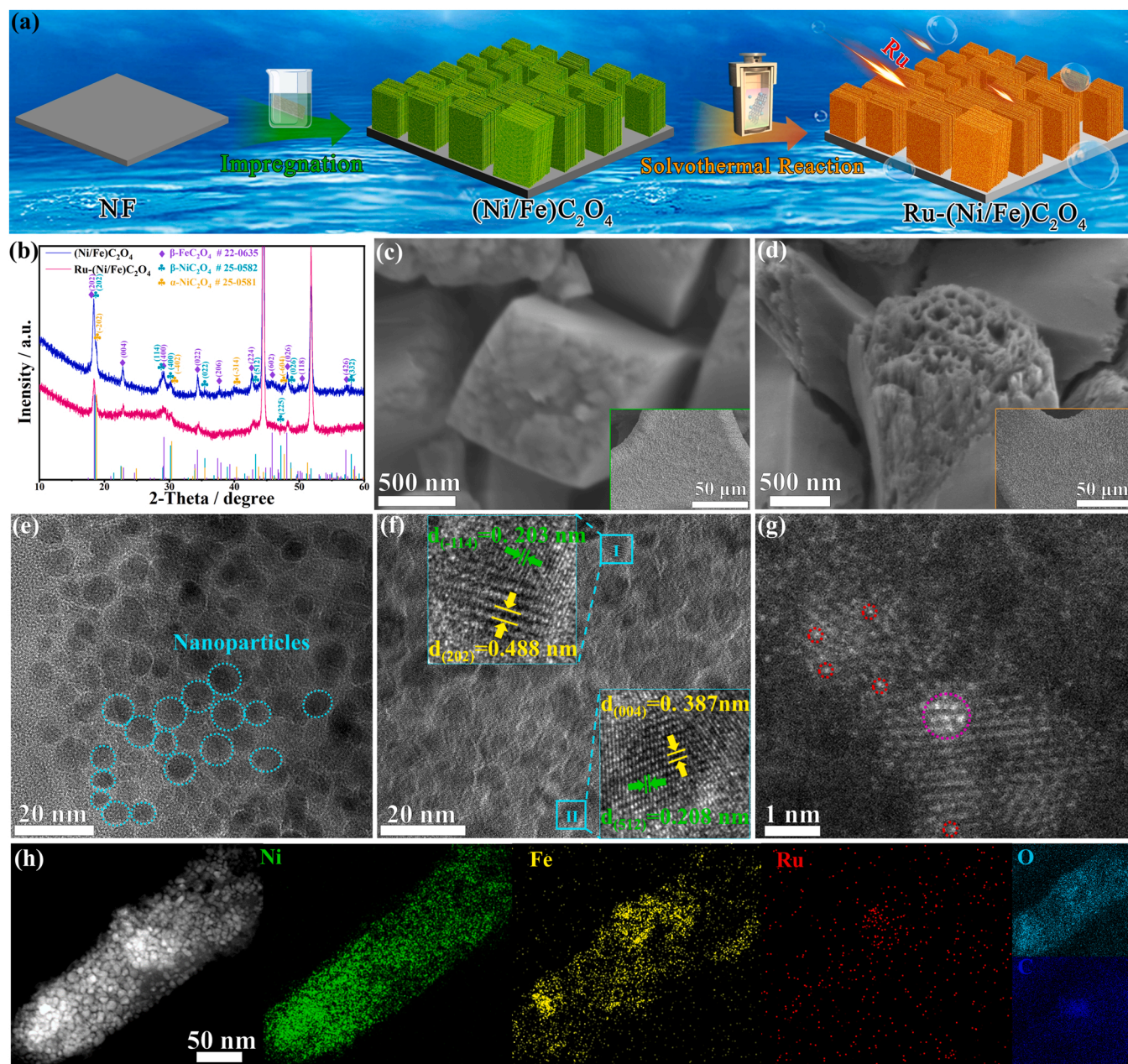


**Fig. 1.** (a) Schematic illustration for fabricating (Ni/Fe) $\text{C}_2\text{O}_4$  and Ru-(Ni/Fe) $\text{C}_2\text{O}_4$ . (b) XRD patterns of (Ni/Fe) $\text{C}_2\text{O}_4$  and Ru-(Ni/Fe) $\text{C}_2\text{O}_4$ . SEM images of (c) (Ni/Fe) $\text{C}_2\text{O}_4$  and (d) Ru-(Ni/Fe) $\text{C}_2\text{O}_4$ . The insets correspond to SEM images with lower magnification. (e) Representative TEM image of (Ni/Fe) $\text{C}_2\text{O}_4$ . (f) TEM and HRTEM image of Ru-(Ni/Fe) $\text{C}_2\text{O}_4$ . (g) AC-HAADF-STEM image of Ru-(Ni/Fe) $\text{C}_2\text{O}_4$ . (h) HAADF-STEM image and the corresponding EDS mapping of Ni, Fe, Ru, O, and C in Ru-(Ni/Fe) $\text{C}_2\text{O}_4$ .

results. Aberration-corrected high-angle annular dark-field scanning transmission electron microscopy (AC-HAADF-STEM) analysis was performed to investigate the distribution of trace Ru species. As visualized in Figs. 1g and S15, the isolated brightest spots, marked with red circles, are designated Ru single atoms, and the pink circle with a size of  $\sim 1$  nm is designated Ru nanoparticles. The coexistence of single Ru sites and Ru nanoparticles in Ru-(Ni/Fe) $\text{C}_2\text{O}_4$  will facilitate the electrocatalytic reaction synergistically [39]. The HAADF image in Fig. 1h also shows the unique microbelts stacked by numerous nanoparticles, and the corresponding EDS result demonstrates the homogeneous distributions of Ni, Fe, Ru, C and O. Inductively coupled plasma optic emission spectrometer (ICP-OES) was shown that the content of Ru is determined to be 0.55 wt%, revealing the ultra-trace amount of Ru in the Ru-(Ni/Fe) $\text{C}_2\text{O}_4$ . Taken together, these results firmly confirm that the

as-synthesized Ru-(Ni/Fe) $\text{C}_2\text{O}_4$  possesses the characteristics of solid-solution-like that contains interlaced HIFs with trace Ru nano-species implanting; meanwhile, Ru-(Ni/Fe) $\text{C}_2\text{O}_4$  displays a multidimensional stacking structure, including nanoparticles (0D), microbelts (2D), and microprisms (3D).

X-ray photoelectron spectroscopy (XPS) was conducted to characterize the electronic structure and chemical composition. The narrow Ru 3p spectrum in Fig. 2a is deconvoluted into two satellite peaks and two prominent peaks centered at 462.2 and 483.9 eV, which can be assigned to  $\text{Ru}^0$  [39,40]. Meanwhile, the peaks at 463.7 and 485.9 eV could be indexed to  $\text{Ru}^{3+}$ , which may result from atomically dispersed Ru atoms that bond with supports. The Ni 2p spectrum of (Ni/Fe) $\text{C}_2\text{O}_4$  in Fig. 2b can be fitted with two Ni doublets, where the peaks at 856.0 and 873.6 eV are assigned to  $\text{Ni}^{2+}$ , and the peaks at 857.4 and 874.9 eV

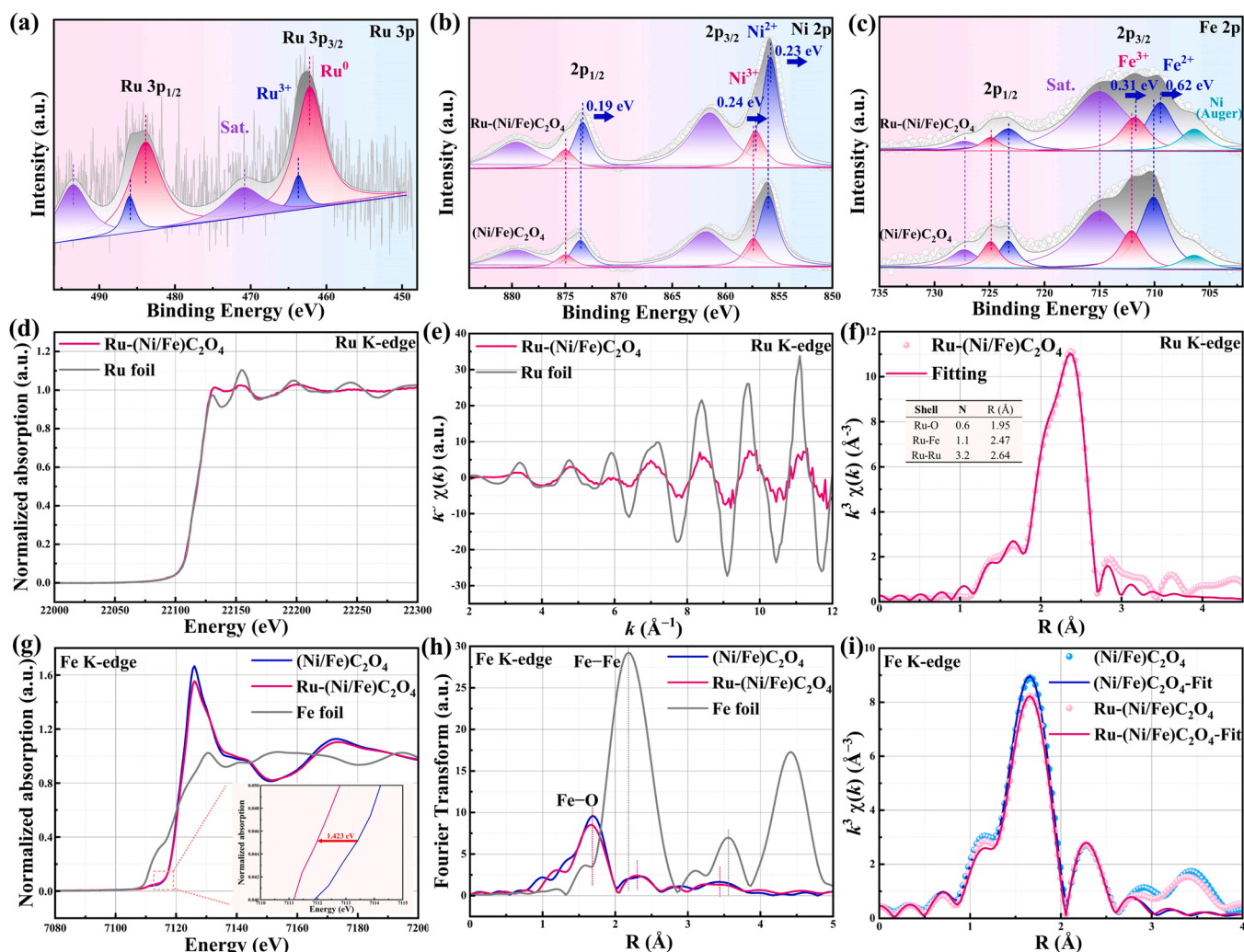


Fig. 2. High-resolution XPS spectra of (a) Ru 3p, (b) Ni 2p, and (c) Fe 2p of (Ni/Fe)C<sub>2</sub>O<sub>4</sub> and Ru-(Ni/Fe)C<sub>2</sub>O<sub>4</sub>. (d) XANES spectra of Ru-(Ni/Fe)C<sub>2</sub>O<sub>4</sub> and (e) Ru K-edge EXAFS oscillations. (f) The experimental and fitting EXAFS curves of Ru-(Ni/Fe)C<sub>2</sub>O<sub>4</sub>. (g) XANES and (h) the corresponding Fourier transform  $k^3$ -weighted EXAFS spectra of (Ni/Fe)C<sub>2</sub>O<sub>4</sub>, Ru-(Ni/Fe)C<sub>2</sub>O<sub>4</sub> and Fe foil. (i) First-shell fitting of EXAFS spectra of (Ni/Fe)C<sub>2</sub>O<sub>4</sub> and Ru-(Ni/Fe)C<sub>2</sub>O<sub>4</sub>.

correspond to Ni<sup>3+</sup> [41,42]. After implanting Ru nanospecies, the peaks of Ni<sup>2+</sup> blueshift to 855.8 and 873.4 eV, while the peaks of Ni<sup>3+</sup> blueshift to 857.2 and 875.0 eV. The similar effect is also observed in the Fe 2p spectrum (Fig. 2c). For Fe 2p<sub>3/2</sub>, the peak of Fe<sup>3+</sup> (712.1 eV) shifts to 711.7 eV, and the peak of Fe<sup>2+</sup> (710.1 eV) shifts to 709.5 eV, indicating that there is a strong electronic interaction between Ru and (Ni/Fe)C<sub>2</sub>O<sub>4</sub>, and the electrons transfer from Ru to Ni and Fe. Generally, the negative potential of metal sites is beneficial for the electrocatalytic HER process [43,44]. The XPS analysis of C 1s and O 2p can be found in Fig. S16.

X-ray absorption spectroscopy (XAS) was performed to identify the metal coordination environment. The X-ray near-edge absorption structure (XANES) of the Ru K-edge in Fig. 2d depicts the almost coincident absorption edges of Ru-(Ni/Fe)C<sub>2</sub>O<sub>4</sub> and Ru foil, which implies the main existence of the Ru metal phase, in conformity with the above XPS results. The oscillation curve in Fig. 2e shows that the amplitude of Ru-(Ni/Fe)C<sub>2</sub>O<sub>4</sub> is much smaller than that of Ru foil, shedding light on the small size of Ru species [45]. Furthermore, the ARTEMIS module is used to fit the first-shell peak of the EXAFS spectra [46]. As fitted in Fig. 2f and Table S1, Ru mainly bonds with Ru and partly bonds with transition metals (M = Fe or Ni, hereinafter), suggesting the coexistence of Ru single atoms and Ru particles, which is in good agreement with the above AC-STEM observations. The existence of Ru-M suggests a strong interaction between C<sub>2</sub>O<sub>4</sub><sup>2-</sup> and Ru<sup>3+</sup>, following the equation ( $3\text{C}_2\text{O}_4^{2-} +$

$2\text{Ru}^{3+} \rightarrow 2\text{Ru} + 6\text{CO}_2$ ). Additionally, the formation of Ru-M would avoid the dissolution of M in the hybrid electrolyzer [47]. To avoid the influence of NF, XAS of Fe is conducted to reveal the coordination state of Ni and Fe sites due to the nearly identical microstructures of NiC<sub>2</sub>O<sub>4</sub> and FeC<sub>2</sub>O<sub>4</sub>. The normalized XANES spectra of the Fe K-edge in Fig. 2g show that the absorption edge shifts by ~1.42 eV toward lower energy, and the white-line intensity decreases after Ru implanting, suggesting the slightly decreased valence state of Fe, which implies less charge transfer from Fe to the nearby O atoms due to the consumption of partial C<sub>2</sub>O<sub>4</sub><sup>2-</sup> [48]. The Fourier transformed (FT)  $k^3$ -weighted EXAFS spectrum in Fig. 2h presents one main peak at 1.67 Å (Fe-O coordination), while no obvious peaks at 2.18 Å (Fe-Fe coordination) are detected, indicating that Fe species are atomically dispersed in (Ni/Fe)C<sub>2</sub>O<sub>4</sub> and Ru-(Ni/Fe)C<sub>2</sub>O<sub>4</sub>. This unique structural advantage of oxalate effectively inhibits the agglomeration of metal centers. The oscillations in Fig. S17 exhibit smaller amplitude oscillations of Ru-(Ni/Fe)C<sub>2</sub>O<sub>4</sub> than (Ni/Fe)C<sub>2</sub>O<sub>4</sub>, demonstrating the decreased coordination number of Fe species after loading Ru nanospecies. The fitted EXAFS spectra in Fig. 2i and Table S2 show that the coordination numbers of both Fe-O and Fe-C decrease after Ru loading, further corroborating the consumption of partial C<sub>2</sub>O<sub>4</sub><sup>2-</sup> during the incorporation of Ru<sup>3+</sup>, which is consistent with the above mechanism. Based on the above analysis, trace Ru nanospecies are implanted in the Ni/Fe-based oxalate solid-solution-like by reacting with partial C<sub>2</sub>O<sub>4</sub><sup>2-</sup>, which is beneficial for dispersing Ru nanospecies and



thus regulating the electronic structure of Ni and Fe, stabilizing the structure of (Ni/Fe) $\text{C}_2\text{O}_4$  by the formation of Ru–M bonds.

### 3.2. Electrocatalytic cathodic reaction

The electrocatalytic HER activity of Ru-(Ni/Fe) $\text{C}_2\text{O}_4$  was investigated using a typical three-electrode apparatus in 1 M KOH. The cathodic polarization curves in Fig. 3a show that Ru-(Ni/Fe) $\text{C}_2\text{O}_4$  requires a relatively low overpotential of 42 mV to reach a current density of  $10 \text{ mA cm}^{-2}$ , superior to that of NF (282 mV), (Ni/Fe) $\text{C}_2\text{O}_4$  (246 mV), and Ru-NF (101 mV). Remarkably, Ru-(Ni/Fe) $\text{C}_2\text{O}_4$  exhibits a much lower overpotential of 323 mV at a large current density of  $500 \text{ mA cm}^{-2}$ , which is close to state-of-the-art Pt/C (322 mV). The kinetics of the HER process are evaluated based on Tafel slopes, as plotted in Fig. 3b. Ru-(Ni/Fe) $\text{C}_2\text{O}_4$  manifests the lowest Tafel slope of  $39 \text{ mV dec}^{-1}$ , verifying a favorable Volmer-Heyrovsky mechanism, where the dissociation of water is the rate-determining step [49,50]. Accordingly, exchange current density ( $j_0$ ) is calculated in Table S3, and the  $j_0$  of Ru-(Ni/Fe) $\text{C}_2\text{O}_4$  is determined to be  $2.874 \text{ mA cm}^{-2}$ , 11 times larger than that of (Ni/Fe) $\text{C}_2\text{O}_4$  ( $0.2552 \text{ mA cm}^{-2}$ ), demonstrating the obvious

enhancement of the inherent HER activity after loading Ru nanospecies. The superiority in the HER activity of Ru-(Ni/Fe) $\text{C}_2\text{O}_4$  compared to those of recently developed nickel/ruthenium-based materials is shown in Fig. 3c and Table S4.

The electrochemical impedance spectra (EIS) at an overpotential of 100 mV are recorded in Fig. 3d, and the inset shows the well-fitted Nyquist plots including the solution resistance ( $R_s$ ), charge transfer resistance ( $R_{ct}$ ) and constant phase angle element (CPE). The  $R_{ct}$  of Ru-(Ni/Fe) $\text{C}_2\text{O}_4$  is estimated to be  $3.26 \Omega$ , far less than that of (Ni/Fe) $\text{C}_2\text{O}_4$  ( $216.99 \Omega$ ), Ru-NF ( $20.63 \Omega$ ) and NF ( $319.83 \Omega$ ), suggesting that the interaction between Ru and (Ni/Fe) $\text{C}_2\text{O}_4$  grants the electrocatalyst a great capability for transporting electrons across the electrode/electrolyte. The electrochemical surface area (ECSA) is then appraised by measuring the double-layer capacitance ( $C_{dl}$ ) to gain insight into the origin of the enhanced HER activity, as illustrated in Figs. 3e and S18. The  $C_{dl}$  of Ru-(Ni/Fe) $\text{C}_2\text{O}_4$  ( $114.5 \text{ mF cm}^{-2}$ ) is appreciably larger than those of (Ni/Fe) $\text{C}_2\text{O}_4$  ( $2.1 \text{ mF cm}^{-2}$ ) and Ru-NF ( $3.6 \text{ mF cm}^{-2}$ ). The ECSA of Ru-(Ni/Fe) $\text{C}_2\text{O}_4$  is calculated to be  $2862.5 \text{ cm}^2_{\text{ECSA}}$ , which is 31.8 times larger than that of Ru-NF ( $90.0 \text{ cm}^2_{\text{ECSA}}$ ), suggesting that the multidimensional (Ni/Fe) $\text{C}_2\text{O}_4$  nanostructure facilitates dispersing and

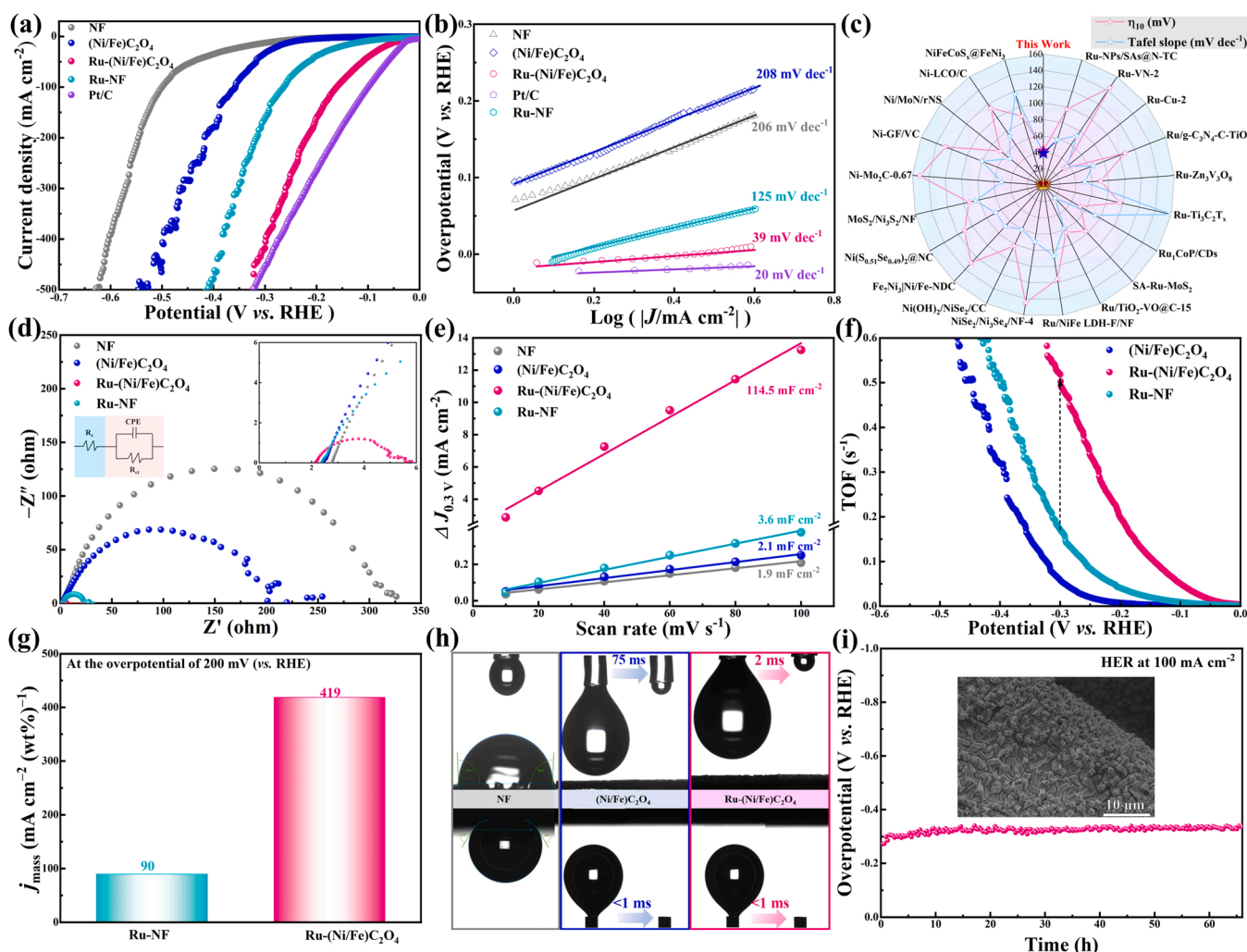


**Fig. 3.** (a) Linear sweep voltammograms of HER for NF, (Ni/Fe) $\text{C}_2\text{O}_4$ , Ru-(Ni/Fe) $\text{C}_2\text{O}_4$ , Ru-NF and Pt/C electrodes in 1 M KOH with 85% iR-corrected. (b) Tafel plots of the above materials. (c) Comparisons of overpotentials for Ru-(Ni/Fe) $\text{C}_2\text{O}_4$  with the recently reported catalysts. (d) Nyquist plots for NF, (Ni/Fe) $\text{C}_2\text{O}_4$ , Ru-(Ni/Fe) $\text{C}_2\text{O}_4$ , and Ru-NF at the overpotential of 100 mV. The inset shows the partial enlargement and the simulated equivalent circuit. (e) Electrochemical double-layer capacitance ( $C_{dl}$ ) values calculated by the current density versus scan rate at 0.3 V. (f) The TOF curves of (Ni/Fe) $\text{C}_2\text{O}_4$ , Ru-(Ni/Fe) $\text{C}_2\text{O}_4$ , and Ru-NF. (g) Calculated mass activity of Ru-NF and Ru-(Ni/Fe) $\text{C}_2\text{O}_4$ . (h) Air-bubble contact angles underwater (top) and water-droplet contact angles (bottom) of NF (gray), (Ni/Fe) $\text{C}_2\text{O}_4$  (blue), Ru-(Ni/Fe) $\text{C}_2\text{O}_4$  (pink). (i) Chronopotentiometry curve of Ru-(Ni/Fe) $\text{C}_2\text{O}_4$  at the constant current density of  $100 \text{ mA cm}^{-2}$  (without iR compensation). The inset is the SEM image of Ru-(Ni/Fe) $\text{C}_2\text{O}_4$  after long-term HER stability.

exposing Ru nanospecies to a greater extent. The turnover frequency (TOF) is calculated to probe the inherent HER performance (Figs. 3f and S19). The TOF value of Ru-(Ni/Fe) $\text{C}_2\text{O}_4$  is  $0.5172 \text{ s}^{-1}$  at an overpotential of 300 mV, which is almost 3-fold higher than that of Ru-NF ( $0.1693 \text{ s}^{-1}$ ), confirming the evidently enhanced electrocatalytic activity achieved by implanting trace Ru nanospecies into hierarchical (Ni/Fe) $\text{C}_2\text{O}_4$ . Moreover, the utilization efficiency of Ru is assessed by mass activity at a potential of  $-0.2 \text{ V}$  (Fig. 3g). The mass activity of Ru-(Ni/

Fe) $\text{C}_2\text{O}_4$  reaches  $419 \text{ mA cm}^{-2} (\text{wt}\%)^{-1}$ , which is 4.6 times higher than that of Ru-NF ( $90 \text{ mA cm}^{-2} (\text{wt}\%)^{-1}$ ), signifying that integrating Ru nanospecies with NiFe-based HIFs evidently enhances the intrinsic activity of noble metal Ru.

Noteworthy, Ru-(Ni/Fe) $\text{C}_2\text{O}_4$  displays a minimum fluctuation in the amplitude of the measured polarization, particularly at large potentials, which is attributed to the unique nanoarray structure that facilitates rapid bubble desorption. On that account, the contact angle

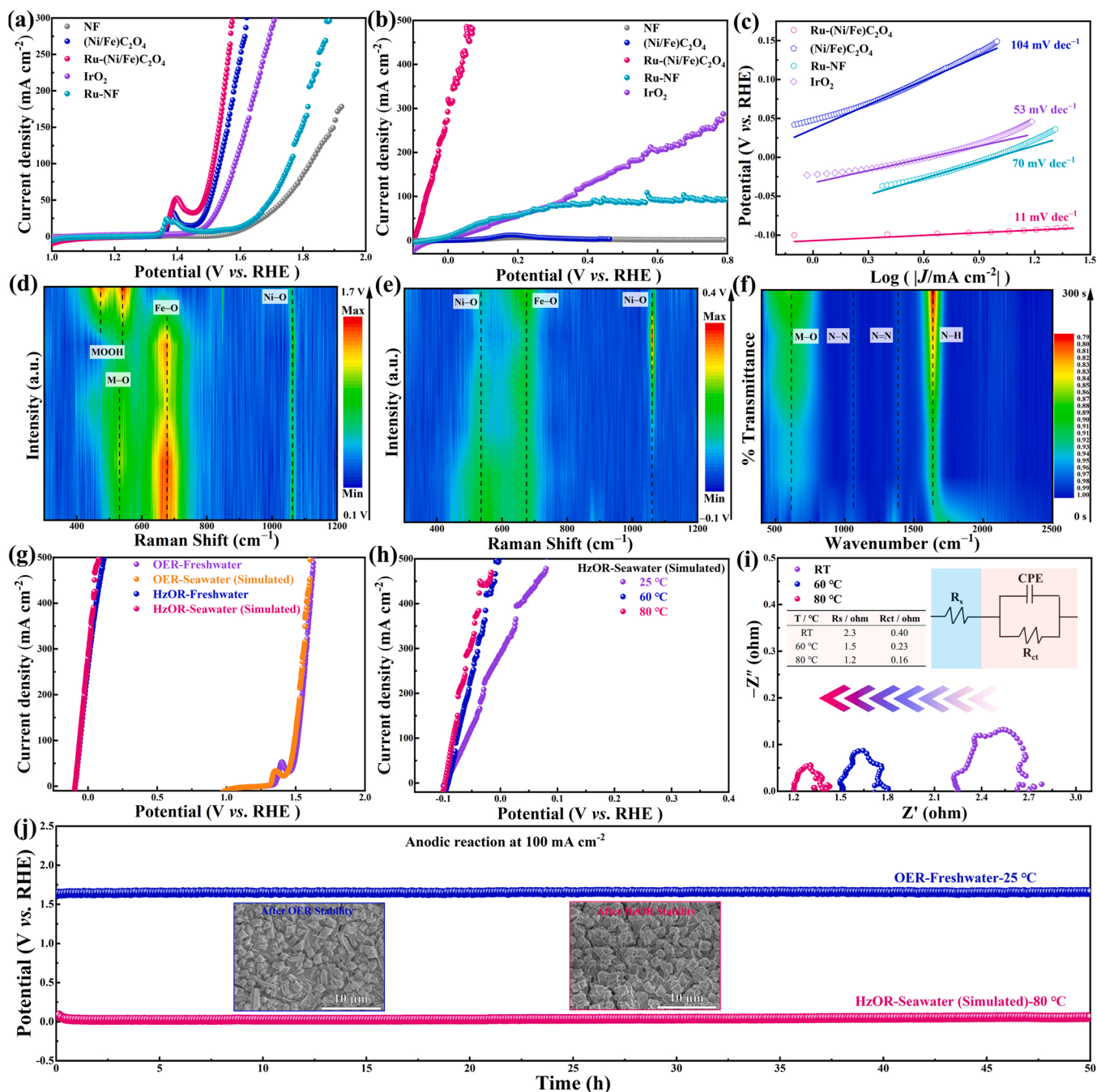


**Fig. 4.** (a) OER polarization curves of NF, (Ni/Fe) $\text{C}_2\text{O}_4$ , Ru-(Ni/Fe) $\text{C}_2\text{O}_4$ , Ru-NF and IrO<sub>2</sub> electrodes in 1 M KOH. (b) HzOR polarization curves and (c) the corresponding Tafel plots of NF, (Ni/Fe) $\text{C}_2\text{O}_4$ , Ru-(Ni/Fe) $\text{C}_2\text{O}_4$ , Ru-NF and IrO<sub>2</sub> in 1 M KOH and 0.1 M N<sub>2</sub>H<sub>4</sub> at 25 °C. (d) In-situ Raman spectra of Ru-(Ni/Fe) $\text{C}_2\text{O}_4$  in 1 M KOH. (e) In-situ Raman spectra of Ru-(Ni/Fe) $\text{C}_2\text{O}_4$  in 1 M KOH and 0.1 M N<sub>2</sub>H<sub>4</sub>. (f) In-situ FTIR spectra of Ru-(Ni/Fe) $\text{C}_2\text{O}_4$  during HzOR process at the constant current density of 100  $\text{mA cm}^{-2}$ . (g) Comparison of HzOR and OER performance for Ru-(Ni/Fe) $\text{C}_2\text{O}_4$  in freshwater and simulated seawater at 25 °C. (h) HzOR performance for Ru-(Ni/Fe) $\text{C}_2\text{O}_4$  in the simulated seawater at 25, 60, and 80 °C under the potential of  $-0.076 \text{ V}$  (vs. RHE). The inset is the equivalent circuit. (i) Nyquist plots of Ru-(Ni/Fe) $\text{C}_2\text{O}_4$  during the HzOR process in the simulated seawater at 25, 60, and 80 °C. The inset is the equivalent circuit. (j) Chronopotentiometry test of Ru-(Ni/Fe) $\text{C}_2\text{O}_4$  for the process of OER in freshwater at 25 °C, and the process of HzOR in simulated seawater at 80 °C (without iR compensation). The inset is the SEM images of Ru-(Ni/Fe) $\text{C}_2\text{O}_4$  after OER and HzOR stability tests.



(CA) of water is measured to explore the infiltration of the electrode/electrolyte contact interface. The sessile drop is first adopted, and some particular moments are recorded in the top of Fig. 3h. The water droplet remains steady on the surface of NF with a constant CA of  $92.4^\circ$ , while the water droplet spreads immediately on Ru-(Ni/Fe) $\text{C}_2\text{O}_4$  within only 2 ms, revealing the superhydrophilic character of Ru-(Ni/Fe) $\text{C}_2\text{O}_4$ . Furthermore, bubble contact underwater is then conducted to probe the ability to desert bubbles (the bottom of Fig. 3h). The air bubble stays stably on the surface of the NF underwater with a large CA of  $124.2^\circ$ . However, air bubbles are difficult to adsorb on (Ni/Fe) $\text{C}_2\text{O}_4$  and Ru-(Ni/Fe) $\text{C}_2\text{O}_4$ , suggesting superaerophobicity. These unique features of Ru-(Ni/Fe) $\text{C}_2\text{O}_4$  may be stem from the hierarchically stacking structure with abundant oxygen-containing functional groups, which governs the efficient transfer of electrolyte and the timely release of gas bubbles during the consecutive HER process [51]. Afterward, the long-term durability is assessed by chronopotentiometry measurement (Fig. 3i). Ru-(Ni/Fe) $\text{C}_2\text{O}_4$  works at a large current density of  $100 \text{ mA cm}^{-2}$  continuously over 65 h without notable attenuation, which implies outstanding electrochemical constancy in alkaline electrolytes. Furthermore, the SEM image in the inset of Fig. 3i verifies the nearly intact morphology of Ru-(Ni/Fe) $\text{C}_2\text{O}_4$  after the long-term stability test, confirming the sturdy structure. In the comparative XPS spectra, no apparent movement of peaks in Ru 3p, Ni 2p and Fe 2p is observed, confirming the robust metal active sites for Ru-(Ni/Fe) $\text{C}_2\text{O}_4$  (Fig. S20). In light of the above, Ru-(Ni/Fe) $\text{C}_2\text{O}_4$  is determined to be a splendid electrocatalyst with trace Ru implanted, which endorses the accessibility of the HER process efficiently, economically, and continuously.

### 3.3. Electrocatalytic anodic reaction

Before exploring the electrocatalytic performance in alkaline seawater, the OER performance of Ru-(Ni/Fe) $\text{C}_2\text{O}_4$  was originally tested (Fig. 4a). (Ni/Fe) $\text{C}_2\text{O}_4$  manifests a potential of 1.504 V (overpotential: 274 mV) at a current density of  $50 \text{ mA cm}^{-2}$ , while the potential decreases to 1.486 V (256 mV) after Ru loading, which outstandingly outperforms commercial  $\text{IrO}_2$  (1.544 V). The Tafel slopes and EIS curves in Figs. S21 and S22 corroborate the superior kinetics of the OER for Ru-(Ni/Fe) $\text{C}_2\text{O}_4$ . Despite the preferable OER performance, a large energy input is still needed. In regard to this, the HzOR is introduced to replace the formidable OER. The Ru-(Ni/Fe) $\text{C}_2\text{O}_4$  electrode exhibits extraordinary HzOR activity, which only requires exceedingly low potentials of  $-0.096 \text{ V}$ ,  $-0.079 \text{ V}$ , and  $-0.062 \text{ V}$  to reach  $10$ ,  $50$  and  $100 \text{ mA cm}^{-2}$ , respectively (Fig. 4b and Table S5). Markedly, the HzOR activity of Ru-(Ni/Fe) $\text{C}_2\text{O}_4$  is also superior to those of transition metal electrocatalysts reported to date (Table S6). As plotted in Figs. S23 and S24, the HzOR performance of Ru-(Ni/Fe) $\text{C}_2\text{O}_4$  possesses good repeatability; in contrast, (Ni/Fe) $\text{C}_2\text{O}_4$  and Ru-NF show quickly diminishing activities, suggesting that implanting Ru nanospecies into the (Ni/Fe) $\text{C}_2\text{O}_4$  solid-solution-like not only ameliorates the catalytic activity but also stabilizes the surface structure. Strikingly, Ru-(Ni/Fe) $\text{C}_2\text{O}_4$  discloses a markedly smaller Tafel slope of  $11 \text{ mV dec}^{-1}$  than (Ni/Fe) $\text{C}_2\text{O}_4$  ( $104 \text{ mV dec}^{-1}$ ), Ru-NF ( $70 \text{ mV dec}^{-1}$ ) and  $\text{IrO}_2$  ( $53 \text{ mV dec}^{-1}$ ), verifying the accelerated HzOR catalytic kinetics, which may be attributed to the effective combination of Ru implanting and HIFs (Fig. 4c). In addition, the EIS in Fig. S25 display the smallest charge-transfer impedance of Ru-(Ni/Fe) $\text{C}_2\text{O}_4$  among the counterparts, which matches well with the results of the HzOR performance.

To reveal the intrinsic active sites and the differences in stability, the in-situ Raman spectrum is recorded during the electrochemical process. The OER process of Ru-(Ni/Fe) $\text{C}_2\text{O}_4$  demonstrates bands at  $529$ ,  $678$  and  $1063 \text{ cm}^{-1}$  that are associated with M–O, Fe–O and Ni–O bonds, respectively (Figs. 4d and S26) [52–54]. When the potential is applied above  $1.4 \text{ V}$ , two strong peaks appear at  $475$  and  $544 \text{ cm}^{-1}$ , coinciding well with MOOH (M=Ni and Fe), which are regarded as OER active sites [55]. The in-situ Raman spectrum of (Ni/Fe) $\text{C}_2\text{O}_4$  in Fig. S27 displays nearly the same reconstruction process, implying that the active sites are

mainly reconstructed from (Ni/Fe) $\text{C}_2\text{O}_4$ . During the subsequent HzOR process, (Ni/Fe) $\text{C}_2\text{O}_4$  shows disappearing bands of active sites, accompanied by the shedding of the electrocatalyst (Fig. S28). Surprisingly, the in-situ Raman spectrum of Ru-(Ni/Fe) $\text{C}_2\text{O}_4$  in Figs. 4e and S29 depicts the gradually intensified bands with the applied voltage, revealing that the active sites are mainly from M–O, which is stable in the presence of  $\text{N}_2\text{H}_4$ . The in-situ FTIR spectrum of Ru-(Ni/Fe) $\text{C}_2\text{O}_4$  in Figs. 4f and S30 shows continuously strong band at  $595 \text{ cm}^{-1}$ , identified as the active site of M–O for HzOR [56]. When the charge applied, the bands at  $1068$ ,  $1392$ , and  $1634 \text{ cm}^{-1}$  appear, which are ascribed to N–N, N=N, and N–H (the intermediate species) due to the partial dehydrogenation of the adsorbed hydrazine [57,58]. In comparison, (Ni/Fe) $\text{C}_2\text{O}_4$  has a moderate IR band of N = N and a gradually waning band of M–O, validating the slow reaction kinetics and unstable active sites in the solution containing  $\text{N}_2\text{H}_4$  (Fig. S31). Thus, the difference in stability should be caused by the formation of a relatively strong Ru–M bond after implanting Ru nanospecies, which is conducive to enhancing the anti-dissolution of M in the presence of  $\text{N}_2\text{H}_4$ .

From the perspective of large-scale electrolysis, the HzOR is performed in simulated seawater, which efficaciously alleviates the allocation problem of freshwater resources, to a certain extent [59]. The performance of the HzOR in seawater is almost the same as that in freshwater, implying that the HzOR with Ru-(Ni/Fe) $\text{C}_2\text{O}_4$  is not interfered by  $\text{Cl}^-$  (Fig. 4g). For comparison, the OER, with a closer onset potential to that of the CLER, also performs well in seawater, corroborating the high selectivity of Ru-(Ni/Fe) $\text{C}_2\text{O}_4$ . Considering the outstanding HzOR performance of Ru-(Ni/Fe) $\text{C}_2\text{O}_4$ , the system is applied under commercial electrolysis conditions, i.e., at industrial electrolysis temperatures ( $60$ – $80^\circ\text{C}$ ) Fig. 4h discloses that the HzOR activity of Ru-(Ni/Fe) $\text{C}_2\text{O}_4$  is improved with increasing temperature, which only requires a low potential of  $-0.083 \text{ V}$  and  $-0.075 \text{ V}$  to deliver  $100 \text{ mA cm}^{-2}$  at  $60^\circ\text{C}$  and  $80^\circ\text{C}$ , respectively [60,61]. Notably, the Nyquist diagram in Fig. 4i shows decreased  $R_s$  and  $R_{ct}$  with increasing temperature, indicating progressively enhanced solution conductivity, fast mass diffusion and charge transfer at the interface of the electrode/electrolyte.

To evaluate the possibility of Ru-(Ni/Fe) $\text{C}_2\text{O}_4$  for practical applications, chronopotentiometry measurements were performed to detect the durability of the HzOR in seawater at  $80^\circ\text{C}$  (Fig. 4j). In sharp comparison, the stability of the regular OER process is tested in  $1 \text{ M KOH}$  at room temperature. The large potential of  $\sim 1.65 \text{ V}$  is continuously required to reach  $100 \text{ mA cm}^{-2}$  during the OER process, which leads to a considerable consumption of energy and freshwater. While conducting the HzOR in seawater at  $80^\circ\text{C}$ , the curve remains steady with negligible decay over 50 h, indicating outstanding durability and strong salt tolerance. In particular, the long-term HzOR process only needs a substantial potential of  $\sim 0.023 \text{ V}$  at  $100 \text{ mA cm}^{-2}$ , much lower than that of OER. The inset shows SEM images of Ru-(Ni/Fe) $\text{C}_2\text{O}_4$  after OER and HzOR stability tests, and the nanoarrays are still preserved under these harsh conditions, verifying the extraordinary stability of the hybrid structure. The XPS spectra in Fig. S32 show no obvious change except for the slight shift caused by the reducibility of  $\text{N}_2\text{H}_4$ . The TEM images in Fig. S33a display the nearly unchanged microbelt structure stacked from nanoparticles. The HRTEM images (Fig. S33b–d) exhibit that HIFs of  $\text{NiC}_2\text{O}_4$  and  $\text{FeC}_2\text{O}_4$  are still retained after the long-term HzOR test, which further corroborates the stability of the structure. These results confidently confirm the serviceable stability of Ru-(Ni/Fe) $\text{C}_2\text{O}_4$  for the alkaline HzOR in seawater at  $80^\circ\text{C}$ , which is essential to propel industrial applications.

### 3.4. HzOR-assisted overall seawater splitting

In light of the outstanding bifunctional feature of Ru-(Ni/Fe) $\text{C}_2\text{O}_4$  for the HER and OER, a two-electrode configuration is assembled to drive overall water splitting. Ru-(Ni/Fe) $\text{C}_2\text{O}_4$ ||Ru-(Ni/Fe) $\text{C}_2\text{O}_4$  demands small voltages of  $1.482$  and  $1.609 \text{ V}$  to reach current densities of  $10$  and

100 mA cm<sup>-2</sup>, respectively, far lower than those of commercial Pt/C||IrO<sub>2</sub> (1.618 V and 1.801 V) (Fig. 5a). Despite the low voltage of Ru-(Ni/Fe)C<sub>2</sub>O<sub>4</sub>||Ru-(Ni/Fe)C<sub>2</sub>O<sub>4</sub>, a large electricity consumption (> 1.4 V) is still needed. In such scenario, HER-HzOR coupled overall seawater electrolysis in Fig. 5b is a promising approach to ease both the energy crisis and freshwater resources. As plotted in Fig. 5c, Ru-(Ni/Fe)C<sub>2</sub>O<sub>4</sub> presents extraordinary activity for overall seawater splitting assisted by hydrazine, which only requires low cell voltages of 0.01, 0.074, and 0.137 V to drive current densities of 10, 50, and 100 mA cm<sup>-2</sup>, respectively, suggesting the huge thermodynamic advantage via HER-HzOR coupling (inset of Fig. 5c). Furthermore, Faradaic efficiency is measured as an intuitive parameter to evaluate the catalytic performance using the water drainage method in an H-type electrolytic cell with 1 M KOH + 0.1 M N<sub>2</sub>H<sub>4</sub> seawater as the electrolyte (Fig. S34) [62, 63]. The volume ratio of H<sub>2</sub> and N<sub>2</sub> is close to 2: 1, implying a high Faradaic efficiency of ~100% for HER-HzOR coupled electrolysis in seawater (Fig. 5d and e). To extend the practicability, the system is operated under industrial electrolysis temperature and the cell voltage decreases with increasing temperature from 25 to 60 and 80 °C (Fig. 5f). The long-term stability of Ru-(Ni/Fe)C<sub>2</sub>O<sub>4</sub> for HER-OER coupling in seawater is evaluated through constant chronopotentiometry at the

current density of 100 mA cm<sup>-2</sup>. As exhibited in Fig. 5g, Ru-(Ni/Fe)C<sub>2</sub>O<sub>4</sub>||Ru-(Ni/Fe)C<sub>2</sub>O<sub>4</sub> exhibits negligible potential degradation after the long-term electrolysis (50 h) for both the process of HER-OER coupling and HER-HzOR coupling, corroborating the stable structure of Ru-(Ni/Fe)C<sub>2</sub>O<sub>4</sub>. Impressively, the cell voltage of HER-HzOR coupled seawater electrolysis only requires 0.300 V, much lower than that of HER-OER coupling (1.882 V). In the long term, the saved electric energy is obviously greater than the value of hydrazine, which can be validated in the part of the Discussion in SI part. The designed system is also measured at quasi-industrial conditions, including a large current density of 500 mA cm<sup>-2</sup> and a high temperature of 80 °C (Fig. 5g and Video 1), and the system can still maintain stability under the harsh conditions. Moreover, the electrolyte after the stability is collected to monitor whether ClO<sup>-</sup> is generated during seawater splitting. The potassium iodide starch paper exhibits no color change in Fig. S35, illustrating that HER-HzOR coupled seawater electrolysis efficiently avoids the occurrence of the CLER, which significantly alleviates corrosion problems that can largely reduce the balance of plant cost [64]. Additionally, the generation of H<sub>2</sub> and N<sub>2</sub> essentially eliminates the possibility of H<sub>2</sub>/O<sub>2</sub> mixing, and the consumption of N<sub>2</sub>H<sub>4</sub> has provided a promising pathway for the fast removal of hydrazine from industrial sewage. Based on the

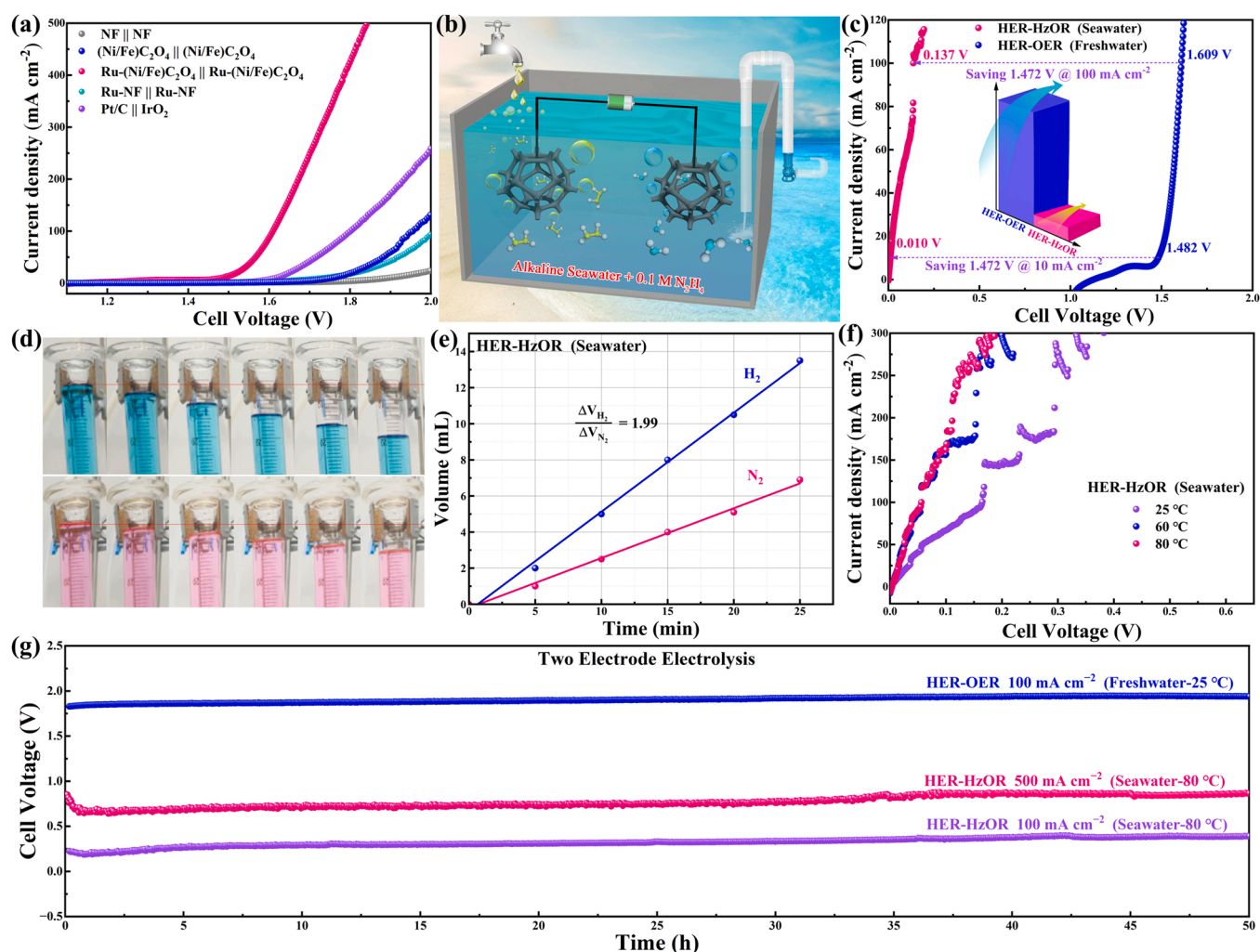


**Fig. 5.** (a) Representative polarization curves for overall water splitting in cells of NF=|NF, (Ni/Fe)C<sub>2</sub>O<sub>4</sub>|(Ni/Fe)C<sub>2</sub>O<sub>4</sub>, Ru-(Ni/Fe)C<sub>2</sub>O<sub>4</sub>||Ru-(Ni/Fe)C<sub>2</sub>O<sub>4</sub>, Ru-NF=|Ru-NF, and Pt/C||IrO<sub>2</sub>, within 1 M KOH electrolyte. (b) Schematic illustration of overall seawater splitting electrolyzer using Ru-(Ni/Fe)C<sub>2</sub>O<sub>4</sub> as both cathode and anode. (c) Comparison of HER-OER coupling in freshwater and HER-HzOR coupling in seawater for Ru-(Ni/Fe)C<sub>2</sub>O<sub>4</sub> at 25 °C. (d) Detail optical images of the measuring gas quantity generated during HER-HzOR coupling electrolysis (the above is H<sub>2</sub>, and the below is N<sub>2</sub>). (e) Diagram of the amount of H<sub>2</sub> and N<sub>2</sub> released over time in 1 M KOH + 0.1 M N<sub>2</sub>H<sub>4</sub> seawater solution. (f) HER-HzOR coupling electrolysis performance for Ru-(Ni/Fe)C<sub>2</sub>O<sub>4</sub> in the simulated seawater at 25, 60, and 80 °C. (g) Chronopotentiometry test of Ru-(Ni/Fe)C<sub>2</sub>O<sub>4</sub> for HER-OER coupling in freshwater at 25 °C, and HER-HzOR coupling in simulated seawater at 80 °C (without iR compensation).



above analysis, Ru-(Ni/Fe)C<sub>2</sub>O<sub>4</sub> is an excellent electrocatalyst for HER-HzOR coupled seawater electrolysis with low cell voltage and long-term stability, which underlines the potential for energy saving, economically beneficial, and easy scaled-up hydrogen production.

Supplementary material related to this article can be found online at [doi:10.1016/j.apcatb.2022.122354](https://doi.org/10.1016/j.apcatb.2022.122354).

### 3.5. Density functional theory calculations

To further investigate the reaction mechanism of the high performance of Ru-(Ni/Fe)C<sub>2</sub>O<sub>4</sub>, the density functional theory (DFT)-based calculations are carried out. To simplify the model, FeC<sub>2</sub>O<sub>4</sub> loaded with Ru cluster structure has been constructed to study the interaction between metal sites, due to the nearly same structure of NiC<sub>2</sub>O<sub>4</sub> and FeC<sub>2</sub>O<sub>4</sub> (Fig. 6a). The charge density difference of Ru-FeC<sub>2</sub>O<sub>4</sub> is calculated to simulate the surface interaction between Ru and Fe (Fig. 6b). As

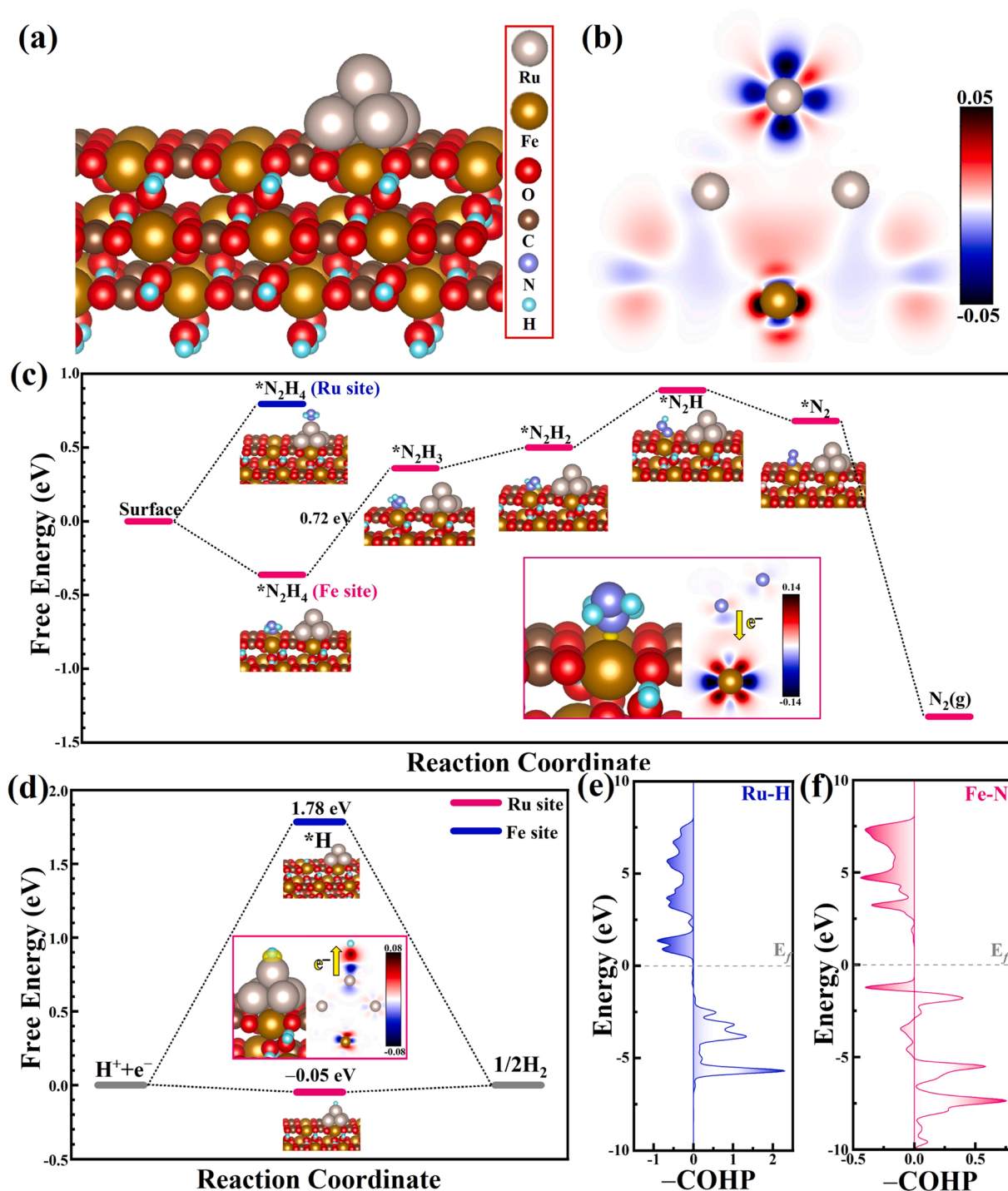


**Fig. 6.** (a) The structure model for Ru-FeC<sub>2</sub>O<sub>4</sub>. (b) The charge density difference analysis for Ru-FeC<sub>2</sub>O<sub>4</sub>. (c) Reaction pathways and free energy profiles of HzOR on the Ru site and Fe site of Ru-FeC<sub>2</sub>O<sub>4</sub>. The inset represents the differential charge density graph of the stable adsorption configurations of N<sub>2</sub>H<sub>4</sub> on Fe site. (d) Free energy profiles of electrocatalytic HER on the Ru site and Fe site of Ru-FeC<sub>2</sub>O<sub>4</sub>. The inset represents the differential charge density graph of the stable adsorption configurations of H on Ru site. COHP calculations of (e) Ru-H bond and (f) Fe-N bond.

expected, an electron accumulation region is observed at the interface of the Ru cluster and Fe site, indicating a strong electron interaction between Ru and  $\text{FeC}_2\text{O}_4$ , which is in line with the above XPS results. Furthermore, the Gibbs free energy is calculated to describe the electrocatalytic activity of metal sites. Generally, HzOR involves four successive dehydrogenation steps ( $\text{*N}_2\text{H}_4 \rightarrow \text{*N}_2\text{H}_3 \rightarrow \text{*N}_2\text{H}_2 \rightarrow \text{*N}_2\text{H} \rightarrow \text{*N}_2$ ), in addition to the adsorption and desorption steps. The adsorption energies of  $\text{N}_2\text{H}_4$  are  $-0.36$  and  $0.80$  eV for the Fe and Ru sites, respectively, indicating that  $\text{N}_2\text{H}_4$  molecules prefer to be adsorbed on the Fe site (Fig. 6c). In the same way, the model of  $\text{NiC}_2\text{O}_4$  loaded with Ru cluster is presented in Fig. S36. The charge density difference in the inset shows that a strong bond is formed between  $\text{N}_2\text{H}_4$  molecule and Fe atom, which ensures the stability of the whole reaction process. Moreover, the dehydrogenation steps in whole process shows the first step ( $\text{*N}_2\text{H}_4 \rightarrow \text{*N}_2\text{H}_3$ ) is regarded as the potential determining step with an energy increase of  $0.72$  eV, while the following steps portray milder reaction processes. Notably, the desorption of the  $\text{N}_2$  molecule presents an energy decrease of  $2.01$  eV, which ensures the continuity of the whole reaction and meanwhile avoids the inactivation of the active site. The HER process is calculated in Fig. 6d, and the overpotentials of Fe and Ru sites are  $1.78$  and  $-0.05$  eV, implying that the HER process mainly occurs at the Ru nanospecies, which is in accordance with the above HER analysis results. Additionally, the Crystal Orbital Hamilton Populations (COHP) calculations are adopted to study the bonding states between the metal sites and intermediates [65]. Few antibonding states are founded for the Ru–H bond, which means that the strong interaction between the  $s$  orbital of H and the  $d$  orbital of Ru provides plenty of electrons from the electrode to promote the HER process (Fig. 6e). In contrast, the Fe–N bond shows few antibonding at  $-1.2$  eV (Fig. 6f). According to the acceptance–donation mechanism, the half-filled  $d$  orbital of Fe bonding with the  $p$  orbital of N atom; and meanwhile, more electrons in the antibonding orbital of the N–N bond are transferred to the metal atom under the electric field, resulting in the dehydrogenation process of  $\text{N}_2\text{H}_4$  [66,67].

#### 4. Conclusion

In summary, we have elaborately synthesized a new electrocatalyst by implanting trace Ru nanospecies into a Ni/Fe-based oxalate solid-solution-like through facile and easy-scale procedures. The (Ni/Fe)  $\text{C}_2\text{O}_4$  is applied to disperse Ru nanospecies; and meanwhile, the Ru nanospecies are implanted into the HIFs to regulate the electronic structure of Ni/Fe and stabilize the structure of (Ni/Fe)  $\text{C}_2\text{O}_4$  by forming Ru–M bonds. Systematic experimental analyses alongside the DFT calculations reveal that the synergistic effect of Ru nanospecies and HIFs from (Ni/Fe)  $\text{C}_2\text{O}_4$  endow Ru-(Ni/Fe)  $\text{C}_2\text{O}_4$  with extraordinary activities of HER and HzOR, accompanied by superior stability. Impressively, the as-obtained Ru-(Ni/Fe)  $\text{C}_2\text{O}_4$  exhibits extraordinary trifunctional activity toward the HER, OER and HzOR in alkaline seawater. Notably, the electrolyzer assembled by Ru-(Ni/Fe)  $\text{C}_2\text{O}_4$  only requires an ultralow voltage of  $0.01$  V to reach  $10 \text{ mA cm}^{-2}$  for overall alkaline seawater splitting assisted by HzOR. Besides, the cell remains stable at a large current density of  $500 \text{ mA cm}^{-2}$  at  $80^\circ\text{C}$  for  $50$  h, almost meeting the requirements for quasi-industrial electrolysis. This work provides a new perspective for designing multifunctional electrocatalysts and develops a promising pathway for overall seawater splitting to achieve a hydrogen economy.

#### CRediT authorship contribution statement

**Jiayang Zhao:** Conceptualization, Methodology, Investigation, Formal analysis, Project administration, Writing—original draft. **Haoran Guo:** Investigation, Software. **Qinghua Zhang:** Materials Characterization. **Yanyan Li:** Resources. **Lin Gu:** Materials Characterization. **Rui Song:** Materials Characterization, Resources, Supervision, Funding acquisition.

#### Declaration of Competing Interest

The authors declare that they have no known competing financial interests or personal relationships that could have appeared to influence the work reported in this paper.

#### Data availability

The authors do not have permission to share data.

#### Acknowledgments

The work is supported by the National Natural Science Foundation of China (Grant Nos. 21875247, 21072221 and 21172252). The authors are also grateful to Prof. Lirong Zheng, Beijing Synchrotron Radiation Facility (BSRF), Institute of High Energy Physics, Chinese Academy of Sciences, for his help in XAS measurement and data analysis.

#### Appendix A. Supplementary material

Supplementary data associated with this article can be found in the online version at doi:10.1016/j.apcatb.2022.122354.

#### References

- [1] J. Wang, Y. Gao, H. Kong, J. Kim, S. Choi, F. Ciucci, Y. Hao, S. Yang, Z. Shao, J. Lim, Non-precious-metal catalysts for alkaline water electrolysis: operando characterizations, theoretical calculations, and recent advances, *Chem. Soc. Rev.* 49 (2020) 9154–9196, <https://doi.org/10.1039/D0CS00575D>.
- [2] M.A. Khan, T. Al-Attas, S. Roy, M.M. Rahman, N. Ghaffour, V. Thangadurai, S. Larter, J. Hu, P.M. Ajayan, M.G. Kibria, Seawater electrolysis for hydrogen production: a solution looking for a problem? *Energy Environ. Sci.* 14 (2021) 4831–4839, <https://doi.org/10.1039/D1EE00870F>.
- [3] B.E. Logan, L. Shi, R. Rossi, Enabling the use of seawater for hydrogen gas production in water electrolyzers, *Joule* 5 (2021) 760–762, <https://doi.org/10.1016/j.joule.2021.03.018>.
- [4] S. Dresch, F. Dionigi, M. Klingenhof, P. Strasser, Direct electrolytic splitting of seawater: opportunities and challenges, *ACS Energy Lett.* 4 (2019) 933–942, <https://doi.org/10.1021/acseenergylett.9b00220>.
- [5] W. Tong, M. Forster, F. Dionigi, S. Dresch, R. Sadeghi Erami, P. Strasser, A.J. Cowan, P. Farràs, Electrolysis of low-grade and saline surface water, *Nat. Energy* 5 (2020) 367–377, <https://doi.org/10.1038/s41560-020-0550-8>.
- [6] H. Wang, L. Chen, H. Pang, S. Kaskel, Q. Xu, MOF-derived electrocatalysts for oxygen reduction, oxygen evolution and hydrogen evolution reactions, *Chem. Soc. Rev.* 49 (2020) 1414–1448, <https://doi.org/10.1039/C9CS00906J>.
- [7] T. Guo, L. Li, Z. Wang, Recent development and future perspectives of amorphous transition metal-based electrocatalysts for oxygen evolution reaction, *Adv. Energy Mater.* 12 (2022), 2200827, <https://doi.org/10.1002/aenm.202200827>.
- [8] M.T. Bender, X. Yuan, K. Choi, Alcohol oxidation as alternative anode reactions paired with (photo)electrochemical fuel production reactions, *Nat. Commun.* 11 (2020) 4594, <https://doi.org/10.1038/s41467-020-18461-1>.
- [9] Y. Xu, B. Zhang, Recent advances in electrochemical hydrogen production from water assisted by alternative oxidation reactions, *ChemElectroChem* 6 (2019) 3214–3226, <https://doi.org/10.1002/celec.201900675>.
- [10] Q. Qian, J. Zhang, J. Li, Y. Li, X. Jin, Y. Zhu, Y. Liu, Z. Li, A. El-Harairy, C. Xiao, G. Zhang, Y. Xie, Artificial heterointerfaces achieve delicate reaction kinetics towards hydrogen evolution and hydrazine oxidation catalysis, *Angew. Chem. Int. Ed.* 60 (2021) 5984–5993, <https://doi.org/10.1002/anie.202014362>.
- [11] N.K. Katiyar, S. Dhakar, A. Parui, P. Gakhad, A.K. Singh, K. Biswas, C.S. Tiwary, S. Sharma, Electrooxidation of hydrazine utilizing high-entropy alloys: assisting the oxygen evolution reaction at the thermodynamic voltage, *ACS Catal.* 11 (2021) 14000–14007, <https://doi.org/10.1021/acscatal.1c03571>.
- [12] Y. Zhu, J. Zhang, Q. Qian, Y. Li, Z. Li, Y. Liu, C. Xiao, G. Zhang, Y. Xie, Dual nanoislands on Ni/C hybrid nanosheet activate superior hydrazine oxidation-assisted high-efficiency  $\text{H}_2$  production, *Angew. Chem. Int. Ed.* 61 (2022), e202113082, <https://doi.org/10.1002/anie.202113082>.
- [13] Z. Yu, J. Xu, L. Meng, L. Liu, Efficient hydrogen production by saline water electrolysis at high current densities without the interfering chlorine evolution, *J. Mater. Chem. A* 9 (2021) 22248–22253, <https://doi.org/10.1039/D1TA05703K>.
- [14] Y. Yan, J. Zhang, X. Shi, Y. Zhu, C. Xia, S. Zaman, X. Hu, X. Wang, B.Y. Xia, A zeolitic-imidazole framework-derived trifunctional electrocatalyst for hydrazine fuel cells, *ACS Nano* 15 (2021) 10286–10295, <https://doi.org/10.1021/acsnano.1c02440>.
- [15] Y. Wang, L. Wan, P. Cui, L. Tong, Y. Ke, T. Sheng, M. Zhang, S. Sun, H. Liang, Y. Wang, K. Zaghbi, H. Wang, Z. Zhou, J. Yuan, Porous carbon membrane-supported atomically dispersed pyrrole-type Fe–N<sub>4</sub> as active sites for electrochemical hydrazine oxidation reaction, *Small* 16 (2020), 2002203, <https://doi.org/10.1002/smll.202002203>.



- [16] J. Li, Y. Li, J. Wang, C. Zhang, H. Ma, C. Zhu, D. Fan, Z. Guo, M. Xu, Y. Wang, H. Ma, Elucidating the critical role of ruthenium single atom sites in water dissociation and dehydrogenation behaviors for robust hydrazine oxidation-boosted alkaline hydrogen evolution, *Adv. Funct. Mater.* 32 (2022), 2109439, <https://doi.org/10.1002/adfm.202109439>.
- [17] J. Zhao, Y. Zeng, J. Wang, Q. Xu, R. Chen, H. Ni, G.J. Cheng, Ultrahigh electrocatalytic activity with trace amounts of platinum loadings on free-standing mesoporous titanium nitride nanotube arrays for hydrogen evolution reactions, *Nanoscale* 12 (2020) 15393–15401, <https://doi.org/10.1039/D0NR01316A>.
- [18] T. Wang, Q. Wang, Y. Wang, Y. Da, W. Zhou, Y. Shao, D. Li, S. Zhan, J. Yuan, H. Wang, Atomically dispersed semimetallic selenium on porous carbon membrane as an electrode for hydrazine fuel cells, *Angew. Chem. Int. Ed.* 58 (2019) 13466–13471, <https://doi.org/10.1002/anie.201907752>.
- [19] J. Zhang, X. Cao, M. Guo, H. Wang, M. Saunders, Y. Xiang, S.P. Jiang, S. Lu, Unique Ni crystalline core/Ni phosphide amorphous shell heterostructured electrocatalyst for hydrazine oxidation reaction of fuel cells, *ACS Appl. Mater. Interfaces* 11 (2019) 19048–19055, <https://doi.org/10.1021/acsami.9b00878>.
- [20] L. Lei, D. Huang, C. Zhou, S. Chen, X. Yan, Z. Li, W. Wang, Demystifying the active roles of NiFe-based oxides/(oxy)hydroxides for electrochemical water splitting under alkaline conditions, *Coord. Chem. Rev.* 408 (2020), 213177, <https://doi.org/10.1016/j.ccr.2019.213177>.
- [21] S. Yang, R. Du, Y. Yu, Z. Zhang, F. Wang, One-step electrodeposition of carbon quantum dots and transition metal ions for N-doped carbon coupled with NiFe oxide clusters: a high-performance electrocatalyst for oxygen evolution, *Nano Energy* 77 (2020), 105057, <https://doi.org/10.1016/j.nanoen.2020.105057>.
- [22] G. Chen, T. Wang, J. Zhang, P. Liu, H. Sun, X. Zhuang, M. Chen, X. Feng, Accelerated hydrogen evolution kinetics on NiFe-layered double hydroxide electrocatalysts by tailoring water dissociation active sites, *Adv. Mater.* 30 (2018), 1706279, <https://doi.org/10.1002/adma.201706279>.
- [23] Y. Ma, D. Liu, H. Wu, M. Li, S. Ding, A.S. Hall, C. Xiao, Promoting bifunctional water splitting by modification of the electronic structure at the interface of NiFe layered double hydroxide and Ag, *ACS Appl. Mater. Interfaces* 13 (2021) 26055–26063, <https://doi.org/10.1021/acsami.1c05123>.
- [24] S. Suárez García, R. Solórzano, F. Novio, R. Alibés, F. Busqué, D. Ruiz Molina, Coordination polymers nanoparticles for bioimaging, *Coord. Chem. Rev.* 432 (2021), 213716, <https://doi.org/10.1016/j.ccr.2020.213716>.
- [25] T. Yamada, M. Sadakiyo, H. Kitagawa, High proton conductivity of one-dimensional ferrous oxalate dihydrate, *J. Am. Chem. Soc.* 131 (2009) 3144–3145, <https://doi.org/10.1021/ja808681m>.
- [26] F. Liu, X. Jiang, H. Wang, C. Chen, Y. Yang, T. Sheng, Y. Wei, X. Zhao, L. Wei, Boosting electrocatalytic hydrazine oxidation reaction on high-index faceted Au concave trioctahedral nanocrystals, *ACS Sustain. Chem. Eng.* 10 (2022) 696–702, <https://doi.org/10.1021/acssuschemeng.1c07700>.
- [27] Y. Wang, P. Zheng, M. Li, Y. Li, X. Zhang, J. Chen, X. Fang, Y. Liu, X. Yuan, X. Dai, H. Wang, Interfacial synergy between dispersed Ru sub-nanoclusters and porous NiFe layered double hydroxide on accelerated overall water splitting by intermediate modulation, *Nanoscale* 12 (2020) 9669–9679, <https://doi.org/10.1039/D0NR01491E>.
- [28] L. Huang, H. Lin, C.Y. Zheng, E.J. Kluender, R. Golnabi, B. Shen, C.A. Mirkin, Multimetallic high-index faceted heterostructured nanoparticles, *J. Am. Chem. Soc.* 142 (2020) 4570–4575, <https://doi.org/10.1021/jacs.0c00045>.
- [29] L. Huang, M. Liu, H. Lin, Y. Xu, J. Wu, V.P. Dravid, C.A. Mirkin, Shape regulation of high-index facet nanoparticles by dealloying, *Science* 365 (2019) 1159–1163, <https://doi.org/10.1126/science.aax5843>.
- [30] H. Fang, D. Liu, Y. Luo, Y. Zhou, S. Liang, X. Wang, B. Lin, L. Jiang, Challenges and opportunities of Ru-based catalysts toward the synthesis and utilization of ammonia, *ACS Catal.* 12 (2022) 3938–3954, <https://doi.org/10.1021/acscatal.2c00090>.
- [31] K. Seth, A.J. Darling, C.F. Holder, Y. Xiong, J.R. Shallenberger, R.E. Schaak, In situ evolution of Ru<sub>4</sub>Al<sub>13</sub> crystals into a highly active catalyst for the hydrogen evolution reaction, *Chem. Mater.* 33 (2021) 7124–7131, <https://doi.org/10.1021/acs.chemmater.1c02583>.
- [32] Y. Li, Y. Sun, Y. Qin, W. Zhang, L. Wang, M. Luo, H. Yang, S. Guo, Recent advances on water-splitting electrocatalysis mediated by noble-metal-based nanostructured materials, *Adv. Energy Mater.* 10 (2020), 1903120, <https://doi.org/10.1002/aenm.201903120>.
- [33] Z. Liu, B. Li, Y. Feng, D. Jia, C. Li, Q. Sun, Y. Zhou, Strong electron coupling of Ru and vacancy-rich carbon dots for synergistically enhanced hydrogen evolution reaction, *Small* 17 (2021), 2102496, <https://doi.org/10.1002/smll.202102496>.
- [34] K. Zhang, Y. Li, X. Hu, F. Liang, L. Wang, R. Xu, Y. Dai, Y. Yao, Inhibitive role of crystal water on lithium storage for multilayer FeC<sub>2</sub>O<sub>4</sub>·xH<sub>2</sub>O anode materials, *Chem. Eng. J.* 404 (2021), 126464, <https://doi.org/10.1016/j.ccej.2020.126464>.
- [35] X. Wang, P. He, Y. Yang, F. Zhang, J. Tang, R. Que, In situ synthesis of Fe-doped NiC<sub>2</sub>O<sub>4</sub> nanorods for efficient oxygen evolution activity and overall water splitting, *Electrochim. Acta* 345 (2020), 136228, <https://doi.org/10.1016/j.electacta.2020.136228>.
- [36] Y. Qiu, Q. Shi, W. Wang, S. Xia, H. Dai, H. Yin, Z. Yang, P. Wang, Facile synthesis of highly dispersed and well-ordered bimetallic nanoparticles on oxide support, *Small* (2022), 2106143, <https://doi.org/10.1002/smll.202106143>.
- [37] K. Li, Y. Liang, J. Yang, G. Yang, H. Zhang, K. Wang, R. Xu, X. Xie, Glucose-induced fabrication of Bi/α-FeC<sub>2</sub>O<sub>4</sub>·2H<sub>2</sub>O heterojunctions: a bifunctional catalyst with enhanced photocatalytic and Fenton oxidation efficiency, *Catal. Sci. Technol.* 9 (2019) 2543–2552, <https://doi.org/10.1039/C9CY00439D>.
- [38] L. Wang, R. Zhang, Y. Jiang, H. Tian, Y. Tan, K. Zhu, Z. Yu, W. Li, Interfacial synthesis of micro-cuboid Ni<sub>0.55</sub>Co<sub>0.45</sub>C<sub>2</sub>O<sub>4</sub> solid solution with enhanced electrochemical performance for hybrid supercapacitors, *Nanoscale* 11 (2019) 13894–13902, <https://doi.org/10.1039/C9NR03790J>.
- [39] Q. He, Y. Zhou, H. Shou, X. Wang, P. Zhang, W. Xu, S. Qiao, C. Wu, H. Liu, D. Liu, S. Chen, R. Long, Z. Qi, X. Wu, L. Song, Synergic reaction kinetics over adjacent ruthenium sites for superb hydrogen generation in alkaline media, *Adv. Mater.* 34 (2022), 2110604, <https://doi.org/10.1002/adma.202110604>.
- [40] P. Su, W. Pei, X. Wang, Y. Ma, Q. Jiang, J. Liang, S. Zhou, J. Zhao, J. Liu, G.Q. Lu, Exceptional electrochemical HER performance with enhanced electron transfer between Ru nanoparticles and single atoms dispersed on a carbon substrate, *Angew. Chem. Int. Ed.* 60 (2021) 16044–16050, <https://doi.org/10.1002/anie.202103557>.
- [41] J. Zhao, Y. Zhang, H. Guo, J. Ren, H. Zhang, Y. Wu, R. Song, Defect-rich Ni(OH)<sub>2</sub>/NiO regulated by WO<sub>3</sub> as core-shell nanoarrays achieving energy-saving water-to-hydrogen conversion via urea electrolysis, *Chem. Eng. J.* 433 (2022), 134497, <https://doi.org/10.1016/j.ccej.2022.134497>.
- [42] B. Song, K. Li, Y. Yin, T. Wu, L. Dang, M. CabánAcedo, J. Han, T. Gao, X. Wang, Z. Zhang, J.R. Schmidt, P. Xu, S. Jin, Tuning mixed nickel iron phosphosulfide nanosheet electrocatalysts for enhanced hydrogen and oxygen evolution, *ACS Catal.* 7 (2017) 8549–8557, <https://doi.org/10.1021/acscatal.7b02575>.
- [43] Y. Li, J. Li, Q. Qian, X. Jin, Y. Liu, Z. Li, Y. Zhu, Y. Guo, G. Zhang, Superhydrophilic Ni-based multicomponent nanorod-confined-nanoflake array electrode achieves waste-battery-driven hydrogen evolution and hydrazine oxidation, *Small* 17 (2021), 2008148, <https://doi.org/10.1002/smll.202008148>.
- [44] Y. Kuang, G. Feng, P. Li, Y. Bi, Y. Li, X. Sun, Single-crystalline ultrathin nickel nanosheets array from insitu topotactic reduction for active and stable electrocatalysis, *Angew. Chem. Int. Ed.* 55 (2016) 693–697, <https://doi.org/10.1002/anie.201509616>.
- [45] K. Kishida, M. Kitano, Y. Inoue, M. Sasase, T. Nakao, T. Tada, H. Abe, Y. Niwa, T. Yokoyama, M. Hara, H. Hosono, Large oblate hemispherical ruthenium particles supported on calcium amide as efficient catalysts for ammonia decomposition, *Chem. Eur. J.* 24 (2018) 7976–7984, <https://doi.org/10.1002/chem.201800467>.
- [46] B. Ravel, M. Newville, ATHENA, ARTEMIS, HEPHAESTUS: data analysis for X-ray absorption spectroscopy using IFFFIT, *J. Synchrotron Radiat.* 12 (2005) 537–541, <https://doi.org/10.1107/s0909049505012719>.
- [47] Y. Wang, H. Zhuo, H. Sun, X. Zhang, X. Dai, C. Luan, C. Qin, H. Zhao, J. Li, M. Wang, J. Ye, S. Sun, Implanting Mo atoms into surface lattice of Pt<sub>3</sub>Mn alloys enclosed by high-indexed facets: promoting highly active sites for ethylene glycol oxidation, *ACS Catal.* 9 (2019) 442–455, <https://doi.org/10.1021/acscatal.8b04447>.
- [48] S. Fang, X. Zhu, X. Liu, J. Gu, W. Liu, D. Wang, W. Zhang, Y. Lin, J. Lu, S. Wei, Y. Li, T. Yao, Uncovering near-free platinum single-atom dynamics during electrochemical hydrogen evolution reaction, *Nat. Commun.* 11 (2020) 1029, <https://doi.org/10.1038/s41467-020-14848-2>.
- [49] X. Zhou, Y. Tian, J. Luo, B. Jin, Z. Wu, X. Ning, L. Zhan, X. Fan, T. Zhou, S. Zhang, X. Zhou, MoC quantum dots@N-doped-carbon for low-cost and efficient hydrogen evolution reaction: from electrocatalysis to photocatalysis, *Adv. Funct. Mater.* (2022), 2201518, <https://doi.org/10.1002/adfm.202201518>.
- [50] J. Fan, X. Cui, S. Yu, L. Gu, Q. Zhang, F. Meng, Z. Peng, L. Ma, J. Ma, K. Qi, Q. Bao, W. Zheng, Interstitial hydrogen atom modulation to boost hydrogen evolution in Pd-based alloy nanoparticles, *ACS Nano* 13 (2019) 12987–12995, <https://doi.org/10.1021/acsnano.9b05615>.
- [51] J. Zhao, Y. Zhang, H. Guo, H. Zhang, J. Ren, R. Song, Rational regulation of crystalline/amorphous microporous nanochannels based on molecular sieve (VSB-5) for electrochemical overall water splitting, *Small* 18 (2022), 2200832, <https://doi.org/10.1002/smll.202200832>.
- [52] D. Thierry, D. Persson, C. Leygraf, N. Boucherit, A. Hugotle Goff, Raman spectroscopy and XPS investigations of anodic corrosion films formed on FeMo alloys in alkaline solutions, *Corros. Sci.* 32 (1991) 273–284, [https://doi.org/10.1016/0010-938X\(91\)90073-X](https://doi.org/10.1016/0010-938X(91)90073-X).
- [53] K.N. Patel, M.P. Deshpande, V.P. Gujarati, S. Pandya, V. Sathe, S.H. Chaki, Structural and optical analysis of Fe doped NiO nanoparticles synthesized by chemical precipitation route, *Mater. Res. Bull.* 106 (2018) 187–196, <https://doi.org/10.1016/j.materresbull.2018.06.003>.
- [54] M.W. Louie, A.T. Bell, An investigation of thin-film Ni-Fe oxide catalysts for the electrochemical evolution of oxygen, *J. Am. Chem. Soc.* 135 (2013) 12329–12337, <https://doi.org/10.1021/ja405351s>.
- [55] Q. Xu, H. Jiang, X. Duan, Z. Jiang, Y. Hu, S.W. Boettcher, W. Zhang, S. Guo, C. Li, Fluorination-enabled reconstruction of NiFe electrocatalysts for efficient water oxidation, *Nano Lett.* 21 (2021) 492–499, <https://doi.org/10.1021/acs.nanolett.0c03950>.
- [56] M. Maruthupandy, G.N. Rajivgandhi, F. Quero, W. Li, Anti-quorum sensing and anti-biofilm activity of nickel oxide nanoparticles against *Pseudomonas aeruginosa*, *J. Environ. Chem. Eng.* 8 (2020), 104533, <https://doi.org/10.1016/j.jece.2020.104533>.
- [57] F. D'Eramo, A.H. Arévalo, J.J. Silber, L. Sereno, Preparation and electrochemical behavior of conducting films obtained by electropolymerization of benzidine in aqueous media, *J. Electroanal. Chem.* 382 (1995) 85–95, [https://doi.org/10.1016/0022-0728\(94\)03668-S](https://doi.org/10.1016/0022-0728(94)03668-S).
- [58] U. Martínez, K. Asazawa, B. Halevi, A. Falase, B. Kiefer, A. Serov, M. Padilla, T. Olson, A. Datye, H. Tanaka, P. Atanassov, Aerosol-derived Ni<sub>1-x</sub>Zn<sub>x</sub> electrocatalysts for direct hydrazine fuel cells, *PCCP* 14 (2012) 5512–5517, <https://doi.org/10.1039/C2CP40546F>.
- [59] S. Wang, P. Yang, X. Sun, H. Xing, J. Hu, P. Chen, Z. Cui, W. Zhu, Z. Ma, Synthesis of 3D heterostructure Co-doped Fe<sub>2</sub>P electrocatalyst for overall seawater

- electrolysis, *Appl. Catal. B Environ.* 297 (2021), 120386, <https://doi.org/10.1016/j.apcatb.2021.120386>.
- [60] X. Liu, R. Guo, K. Ni, F. Xia, C. Niu, B. Wen, J. Meng, P. Wu, J. Wu, X. Wu, L. Mai, Reconstruction-determined alkaline water electrolysis at industrial temperatures, *Adv. Mater.* 32 (2020), 2001136, <https://doi.org/10.1002/adma.202001136>.
- [61] A. Salah, L. Zhang, H. Tan, F. Yu, Z. Lang, N. Alansi, Y. Li, Advanced Ru/Ni/WC@NPC multi-interfacial electrocatalyst for efficient sustainable hydrogen and chlor-alkali co-production, *Adv. Energy Mater.* 12 (2022), 2200332, <https://doi.org/10.1002/aenm.202200332>.
- [62] X. Zhai, Q. Yu, G. Liu, J. Bi, Y. Zhang, J. Chi, J. Lai, B. Yang, L. Wang, Hierarchical microsphere MOF arrays with ultralow Ir doping for efficient hydrogen evolution coupled with hydrazine oxidation in seawater, *J. Mater. Chem. A* 9 (2021) 27424–27433, <https://doi.org/10.1039/D1TA07328A>.
- [63] X. Wang, W. Zhang, Q. Yu, X. Liu, Q. Liang, X. Meng, X. Wang, L. Wang, Fe-doped CoNiP@N-doped carbon nanosheet arrays for hydrazine oxidation assisting energy-saving seawater splitting, *Chem. Eng. J.* 446 (2022), 136987, <https://doi.org/10.1016/j.cej.2022.136987>.
- [64] N. Wen, Y. Xia, H. Wang, D. Zhang, H. Wang, X. Wang, X. Jiao, D. Chen, Large-scale synthesis of spinel  $\text{Ni}_x\text{Mn}_{3-x}\text{O}_4$  solid solution immobilized with iridium single atoms for efficient alkaline seawater electrolysis, *Adv. Sci.* 9 (2022), 2200529, <https://doi.org/10.1002/advs.202200529>.
- [65] V.L. Deringer, A.L. Tchougréeff, R. Dronskowski, Crystal orbital hamilton population (COHP) analysis as projected from plane-wave basis sets, *J. Phys. Chem. A* 115 (2011) 5461–5466, <https://doi.org/10.1021/jp202489s>.
- [66] H. Guo, H. Zhang, J. Zhao, P. Yuan, Y. Li, Y. Zhang, L. Li, S. Wang, R. Song, Two-dimensional  $\text{WO}_3$ -transition-metal dichalcogenide vertical heterostructures for nitrogen fixation: a photo(electro) catalysis theoretical strategy, *J. Phys. Chem. C* 126 (2022) 3043–3053, <https://doi.org/10.1021/acs.jpcc.1c09772>.
- [67] C. Ling, X. Niu, Q. Li, A. Du, J. Wang, Metal-free single atom catalyst for  $\text{N}_2$  fixation driven by visible light, *J. Am. Chem. Soc.* 140 (2018) 14161–14168, <https://doi.org/10.1021/jacs.8b07472>.